



LAWRENCE
LIVERMORE
NATIONAL
LABORATORY

In Operando Soft X-ray Spectroscopy of 3D Graphene Supercapacitor Electrodes

M. Bagge-Hansen, B. C. Wood, T. Ogitsu, T. M. Willey, I. C. Tran, A. Wittstock, M. M. Biener, M. D. Merrill, M. A. Worsley, M. Otani, C. H. Chuang, D. Prendergast, J. Guo, T. F. Baumann, T. van Buuren, J. Biener, J. R. I. Lee

March 20, 2014

Advanced Materials

Disclaimer

This document was prepared as an account of work sponsored by an agency of the United States government. Neither the United States government nor Lawrence Livermore National Security, LLC, nor any of their employees makes any warranty, expressed or implied, or assumes any legal liability or responsibility for the accuracy, completeness, or usefulness of any information, apparatus, product, or process disclosed, or represents that its use would not infringe privately owned rights. Reference herein to any specific commercial product, process, or service by trade name, trademark, manufacturer, or otherwise does not necessarily constitute or imply its endorsement, recommendation, or favoring by the United States government or Lawrence Livermore National Security, LLC. The views and opinions of authors expressed herein do not necessarily state or reflect those of the United States government or Lawrence Livermore National Security, LLC, and shall not be used for advertising or product endorsement purposes.

LLNL-JRNL-652099

Article type: Communication

Potential-induced electronic structure changes in supercapacitor electrodes observed by *in operando* soft x-ray spectroscopy

Authors: *Michael Bagge-Hansen, Brandon C. Wood, Tadashi Ogitsu, Trevor M. Willey, Ich C. Tran, Arne Wittstock, Monika M. Biener, Matthew D. Merrill, Marcus A. Worsley, Minoru Otani, Cheng-Hao Chuang, David Prendergast, Jinghua Guo, Theodore F. Baumann, Tony van Buuren, Jürgen Biener, Jonathan R. I. Lee**

Dr. M. Bagge-Hansen, Dr. B. C. Wood, Dr. T. Ogitsu, Dr. T. M. Willey, Dr. I. C. Tran, Dr. A. Wittstock, Dr. M. M. Biener, Dr. M. D. Merrill, Dr. M. A. Worsley, Dr. T. F. Baumann, Dr. T. van Buuren, Dr. J. Biener, Dr. J. R. I. Lee
Physical and Life Sciences Directorate, Lawrence Livermore National Laboratory, Livermore, California 94550, United States.
Email. lee204@llnl.gov

Dr. M. Otani
Nanosystem Research Institute, National Institute of Advanced Industrial Science and Technology (AIST), Tsukuba, Japan.

Dr. C.-H. Chuang, Dr. J. Guo
Advanced Light Source Division, Lawrence Berkeley National Laboratory, Berkeley, California 94720, United States.

Dr. D. Prendergast
The Molecular Foundry, Materials Sciences Division, Lawrence Berkeley National Laboratory, Berkeley, California 94720, United States.

Keywords: *in operando* x-ray spectroscopy, *ab initio* simulation, supercapacitor, carbon aerogel electrode, electronic structure

Main Text:

Radical improvement of the capacity and efficiency of electrical energy storage systems is needed to meet the burgeoning demands of consumer, industrial, and green technologies.

Electrode/electrolyte interfaces are critical to all electrical energy storage technologies, yet there remains limited understanding of how physiochemical properties of these devices are altered by the interfacial electric field generated during charging. The structural and dynamical responses of the electrolyte to an applied potential have been extensively studied, whereas the analogous responses of the electrode material during operation remain largely unexplored, even for widely used materials such as graphitic electrodes. Herein, we demonstrate that graphene-based supercapacitor electrodes undergo complex, electric-field induced, changes in electronic structure during operation that have their origin in modifications to the electrode surface chemistry and morphology. Atomic-level insight is achieved by combining *in operando* soft x-ray absorption spectroscopy (XAS) with direct *ab initio* simulations of spectral responses under bias. Our results bolster a nascent model in which interfacial capacitance and charge storage are not solely determined by the isolated properties of the electrode and electrolyte, but can be strongly influenced by polarization-induced and electrolyte mediated modifications to the electrode itself^[1, 2].

The core functionality of all electrochemical energy storage systems is strongly influenced by the complex and dynamic behavior of their polarized electrode-electrolyte interfaces. This is especially true for electric double-layer (EDL) capacitors, or supercapacitors, which address a growing need for both rapid charge and discharge while maintaining moderate to high charge storage capability^[3]. In EDL capacitors, electrical energy is stored solely by polarization of the

electrode-electrolyte interface. Accordingly, the desire for dramatically increased capacity and efficiency of EDL capacitors and other electrochemical energy storage systems has motivated extensive research focused on the electrolyte, *i.e.*, transport, proximity, and arrangement of ions approaching the electrode surface. For example, an excellent recent study by Deschamps *et al.*^[4] demonstrates electrolyte reorganization in response to an applied bias, and the groundbreaking work by Chmiola *et al.*^[5] revealed pronounced pore size effects on the interfacial capacity. On the other hand, very little is known about the equally important dynamic physiochemical response of the electrode to charge and discharge, including any electric-field induced changes to the electronic structure during operation. Instead, the electrode is conventionally considered to be static, with charge accumulation or depletion as the only response to polarization of the interface. This lack of understanding of the dynamic physiochemical changes of the electrode is largely due to the paucity of experimental and theoretical methods for characterization of the electrode electronic structure under operating conditions.

Graphitic supercapacitors are ideal model systems to interrogate interfacial phenomena because they are relatively chemically stable, extensively characterized experimentally and theoretically, and are of broad technological interest^[6, 7]. For this study, we use our recently-developed 3D nanographene (3D-NG) bulk electrode material^[8], which has a number of distinct advantages as a model graphitic material. 3D-NG is composed of interconnected single-layer graphene sheets, is binder- and substrate- free, and has a well-characterized hierarchical pore structure (**Figure 1a,b**)^[8, 9]. In contradiction to the generally held perception that graphitic carbon electrodes are electrochemically inert, we demonstrate that these electrodes undergo profound changes in electronic structure under applied voltage bias (Figure 1c,d). Detailed investigation of the

electronic structure reorganization under applied bias is enabled by a recently developed *in operando* soft XAS capability (**Figure S1**), which selectively probes the graphene electrode within the electrode-electrolyte interface (Figure 1b). The resulting XAS data reveal spectral signatures that appear only under applied bias and connote both local geometrical distortion and ion adsorption. A comparison to direct *ab initio* simulations of the XAS spectra from graphene electrodes under bias provides an atomic-level understanding of the observed spectral signatures. The changes in structure and bonding identified within functioning supercapacitors indicate that current charge storage models, such as the conventional rigid band structure model of EDL capacitors, must be revised.

The rigid band structure model assumes that bias-induced electron accumulation/depletion (generally up to ~ 0.01 *e*/carbon atom for graphene electrodes) only shifts the Fermi level without changing the underlying electronic density of states (DOS) of the electrode^[2, 10]. Nonetheless, polarization of the electrode-electrolyte interface generates extremely strong local electric fields ($\sim 10^9$ V/m)^[11] that, in principle, may be capable of perturbing the intrinsic electronic structure, thereby violating the rigid band structure model (Figure 1c). Considering this effect becomes especially important for materials with a low DOS near the Fermi level, such as graphene, where the interfacial capacitance is dominated by the quantum capacitance^[2], and even a small increase in the DOS at the Fermi level would lead to a dramatic increase in the interfacial capacitance. Here, we employ *in operando* XAS as an ideally suited experimental probe of these changes in the DOS since it is element specific and exquisitely sensitive towards subtle changes in bonding and structure (information that cannot be accessed by more traditional characterization techniques)^[12, 13].

In operando C K-edge XAS measurements of 3D-NG EDL capacitor electrodes reveal profound and unexpected changes in the electronic structure of the graphene building blocks upon interfacial charging (**Figure 2**). Specifically, a comparison of the XAS spectra recorded at +250 to +1000 mV in 1M NaCl_(aq) (Figure 2a) with data at 0 mV (Figure 2b) reveals two new resonances at 287.3 eV and ~291 eV (henceforth, α and β , respectively). In contrast, no experimentally significant changes in the XAS spectra were observed under negative bias (Figure 2c, d). The intensities of α and β change systematically with the applied positive bias (**Figure S2 and S3**); however, the dependencies of the two resonances on bias are different (Figure 2e). In addition, α and β dissipate upon removal of the applied bias, indicating that both processes are largely reversible (**Figure S4**). Notably, other spectral features, including the C-C π^* resonance at 285.4eV^[14], remain unchanged to within experimental error, irrespective of the applied bias. Further, both electrochemical characterization (SI section II.2, **Figure S5**) and laser Raman spectroscopy measurements (**Figure S6**) conducted before and after XAS suggest that no deterioration of the 3D-NG electrode or the EDL capacitor performance has occurred as a result of X-ray exposure.

Our discussion of the spectral evolution as a function of time focuses primarily on β at +1000 mV, where statistical confidence is high due to the relatively large intensity changes. The initial response of β is a smooth increase in intensity over ~ 300s until a temporary plateau is reached (Figure 2f). The intensity of β subsequently decreases over a period of tens of minutes, as shown in three sequential spectra at +1000 mV (Figure 2g; α also diminishes, though at a different timescale –**Figure S7 and S8**). The delayed growth and decline imply activated processes, which

may be ion diffusion or changes in conformation. The timescale of the onset behavior is reminiscent of the measured charge times for these materials ^[15], indicating that the initial growth of β is linked to charging dynamics and is thus likely ion-diffusion related. On the other hand, the much longer-timescale decline of β is most probably connected to dissipation of strain energy through broader morphological changes. No significant temporal evolution was identified under any applied negative bias.

Preliminary assignment of α and β is guided by a substantial foundation of carbon XAS. Resonance α resides in an energy range, 286 to 289 eV, largely dominated by σ^* resonances associated with C-X chemistry, where X denotes a specifically adsorbed element or functional group ^[12]. Meanwhile, β falls within a regime, 290 to 293 eV, associated with σ^* features in graphite ^[12, 14, 16]; these resonances are sensitive to modifications in C-C bond geometry, e.g., due to strain or changes in coordination. *Ab initio* simulations were employed to help with the identification of specific charge-induced atomic- and meso-scale phenomena that can explain the observed bias-dependent resonances (see methods). As accounting for the effect of bias is essential, a new theoretical methodology was developed for this study that combines density functional theory-based (DFT) techniques ^[17] for XAS calculation ^[18] with the effective screening medium method ^[2, 19] which inserts into the periodic simulation box a fictitious counter electrode with perfect screening properties (i.e., infinite dielectric constant). Within this framework, the bias is set by adjusting the excess charge on the total system (**Figure S9**). The relative chemical shifts are estimated using the procedure described in reference [20]. ^[20] For simplicity, we base our models on defect-free, single-layer graphene. Because this approach neglects any local heterogeneity that may exist within 3D-NG, we limit our discussion and

analysis to *relative* spectral changes with applied bias, which we assume to be robust with respect to the structural details of the models.

The observation that α appears at 287.3 eV and only under positive bias (Figure 2d) is consistent with specific adsorption of anions on the electrode surface. In a $\text{NaCl}_{(\text{aq})}$ electrolyte, the two most likely candidates are Cl^- and OH^- , yet discrimination between these adsorbants is challenging because the C-Cl and C-OH σ^* resonances can both occur at the relevant energy^[12, 21].

Consequently, we leverage XAS simulations (**Figure 3**) to demonstrate that, of these two ions, only OH^- adsorption exhibits bias-dependent behavior consistent with the experimental data. Specifically, the simulated C-OH σ^* resonance appears in the correct energy window even at low applied bias (see Figure 3 for definition), and shifts negligibly with increasing bias; both features are consistent with Figure 1a. In contrast, the simulated C-Cl σ^* resonance resides in a higher-energy window that would be convolved with the C-C σ^* resonance at lower bias ($\leq +0.0075$ e/atom), yet shifts downward by > 2 eV as the bias is increased. As a result, we conclude that Cl^- adsorption is not appreciable within the potential range we measure. The response to applied bias is also reflected in the C-X bond geometry. For OH^- , short C-X bond distances (1.47-1.52 Å) and near-tetrahedral C-C-X bond angles (108-110°) are predicted for all positive biases, consistent with sp^2 -to- sp^3 rehybridization and substantial covalent character. Meanwhile, the C-Cl σ^* resonance shows no rehybridization/covalency ($\angle\text{C-C-Cl}=90^\circ$) until the excess charge exceeds 0.0075 e/atom and the C-Cl bond length abruptly shortens to < 2.5 Å. The results are consistent with the notion that higher covalency translates to a lower susceptibility to applied bias and also correlates inversely with anion size ($\text{OH}^- < \text{Cl}^-$; **Figure S10**). The charge transfer that

accompanies covalent adsorption of OH^- onto the 3D-NG electrode generates a pseudocapacitive channel for electrical energy storage; the particular sensitivity of XAS provides relatively facile deconvolution of this weak and reversible (Figure S2) faradaic phenomenon from those changes in electronic structure associated with EDL capacitance.

XAS also enables the identification of structural changes associated with EDL formation, which we demonstrate via analysis of β . The energy of β indicates that it is associated with C-C σ^* bonding, and its temporal evolution is consistent with charging dynamics; this assignment is supported by our simulations, from which we infer strain-induced morphological changes in the 3D-NG as the EDL develops during charging. Motivated by recent findings of considerable macroscopic strain effects ($> 2\%$ strain) of graphene-based materials under applied bias ^[15], we simulated spectral response to compressive or tensile stress for a graphene sheet (**Figure 4**). Specifically, two scenarios were explored: in-plane uniaxial strain and local curvature from out-of-plane distortions. The primary spectral response to in-plane tensile (compressive) strain is a red (blue) shift in the position of the dominant C-C σ^* resonance, coupled with minimal variation in intensity (Figure 4a, b). By contrast, change in the local curvature, which we model here by introducing sinusoidal undulations of varying maximal curvature into a graphene sheet (Figure 4c, d), results in a blue (red) shift of the C-C σ^* resonance. The extent of this shift is proportional to the increase (decrease) in local curvature and, by extension, the degree of local compressive (tensile) stress; furthermore, the intensity of the C-C σ^* resonance also decreases (increases) substantially with increasing (decreasing) curvature, a result that is consistent with the existing literature ^[22].

Experimentally, β exhibits both increasing intensity (until the plateau is reached) and a slight red shift with applied positive bias (Figure 2). Although the introduction of in-plane tensile strain could explain the observed red shift (Figure 4b), it does not provide for the observed variation in resonance intensity. Conversely, local planarization of initially curved graphene is entirely consistent with the changes observed in the experimental data under positive bias (including spectra recorded at potentials $< +1000$ mV, see supporting information). As a corollary, local curvature should increase under negative bias; yet, the dependence of β on local curvature is highly non-linear (Figure 4d), with increased curvature inducing far less change in intensity and peak position than would be expected for decreased curvature at positive bias. The spectral response to subtle increases in curvature under negative applied bias could, therefore, fall within experimental error. Indeed, the experimental results at negative bias (Figure 2c) essentially retain the zero-bias position and intensity.

The above analysis strongly suggests that local planarization of initially curved graphene sheets evolves under positive applied bias and is associated with local tensile stress; however, we recently reported that 3D-NG electrodes contract during positive charging, thus indicating a compressive strain state at positive bias^[15]. This apparent discrepancy can be reconciled by assuming a transient strain gradient that reflects the complex kinetics of EDL formation in hierarchal porous electrodes (Figure 4e). Immediately after the application of an applied positive bias, EDL formation/charging occurs preferentially along the pathways that offer the least resistance to ion diffusion (i.e., the surfaces of larger pores)^[7, 23, 24]. Nanometer-scale pores provide much higher resistance toward anion transport, delaying assembly of the equilibrium EDL structure^[24, 25]. During the intermediate stages of charging ($t < \sim 300$ s), it is thus reasonable

to expect nearly complete EDL formation throughout the larger pores and only partial EDL formation within pores of dimensions approaching the EDL thickness. Due to the stiff and non-compliant character of the core of the graphene ligaments in 3D-NG^[8], pores with incomplete EDL formation in this intermediate charging regime will prevent compression of the larger pores that have achieved the complete/equilibrium EDL structure. The suppressed compression is locally experienced as tensile stress between neighboring pores, thereby initiating local planarization of the graphene structures within the macroporous network. Upon full charging, this stress gradient will be partially neutralized, leading to the observed time-dependent dissipation of the β intensity in Figure 2g. This interpretation assigns β to a uniquely mesoscale response, in contrast to the atomic-level response represented by α .

The appearance and rationalization of α and β reveal fundamental and unanticipated complexities in the relationship between electronic and geometric structure in 3D-NG EDL capacitor electrodes. Moreover, the changes indicate structural evolution across multiple length scales (sub-nm- through μm -) during charging, occurring via two independent channels – pseudocapacitive (α) and EDL formation (β). Our findings strongly suggest a more complex understanding of interfacial capacitance in EDL capacitors and further enrich recent literature that proffers similar observations^[26]. Consequently, the results presented in this study emphasize that one cannot assume the capacitance is solely determined by the static electronic structure of the electrode and the thickness of the EDL, but rather must consider the potentially dramatic effects of internal electronic reorganization within the electrode due to strong interfacial interactions. These effects are anticipated to be especially pronounced for electrode materials with a low electronic DOS at the Fermi level or for electrolyte ions that chemically interact with

the electronic states of the electrode. Development of this understanding is enabled by characterizing the 3D-NG under realistic operating environments by combining *in operando* soft XAS with direct simulations of spectral responses under bias. This combined strategy is readily extensible to *in situ/operando* studies of low-Z elements prevalent in systems ranging from energy storage/conversion materials and catalysts to biomaterials.

Experimental Section:

Sample Preparation & Instrumentation: Bulk 3D-NG was prepared according to established protocols^[8] and was employed as both the working electrode (WE) and counter electrode (CE) in all experiments. A fully ultrahigh vacuum compatible electrochemical cell (Figure S1), based upon the design of Guo et al.^[27], was developed to enable *in operando* soft XAS measurements of the 3D-NG WE within a functioning EDLC. A critical design element of the cell is the incorporation of a 100 nm SiN_x window in the outer wall that permits transmission of soft x-rays in to and out of the cell. The WE resides adjacent to this window, thus allowing study of the electrode via *in operando* ‘photon-in, photon-out’ XAS (Figure S1). The specific WE and CE used within a cell were selected to have a volume (/surface) ratio of ~2:1. Within a two-electrode arrangement, the resulting voltage applied across the WE is approximately one third of the total bias applied to the cell, whereas the CE experiences two-thirds of the applied bias. We note, however, that we reference our results in this manuscript to the total bias applied to the cell. Prior to cell assembly, the 3D-NG electrodes were placed under low vacuum within aqueous electrolyte (*i.e.*, 1 M NaCl_(aq)) to promote homogeneous distribution of the solution throughout their porous architecture. Further details of cell construction and assembly are found in the supporting information. All *in operando* XAS measurements were conducted in the total

fluorescence yield (TFY) mode on beamlines 7.0.1.1^[28] and 8.0.1.3^[29] of the Advanced Light Source (ALS), Lawrence Berkeley National Laboratory (LBNL). The experimental end-stations were maintained at base pressures of $\leq 5 \times 10^{-9}$ Torr. Carbon K-edge XAS spectra were energy calibrated to the C(1s) $\rightarrow \pi^*$ resonance of freshly cleaved highly oriented pyrolytic graphite at 285.38 eV^[14]. An I_0 reference signal was obtained simultaneously to each TFY measurement via the drain current from an Au-coated mesh located upstream of the experimental sample. All XAS signals were normalized via a two-stage, ‘double normalization’, process described in the literature and in the SI^[30]. All *in operando* XAS measurements were conducted under potentiostatic conditions, applied via either a potentiostat (BioLogic SP200) or high precision power supply. Subsequent fitting of the normalized XAS spectra was conducted using a custom, quasi-Monte Carlo/random walk, algorithm (see supporting information). Electrochemical characterization (cyclic voltammograms) was conducted using the *in operando* XAS cell in a two-electrode configuration under a 1 M NaCl_(aq) electrolyte.

Computational Methods: Plane-wave DFT calculations^[17] were performed using the Quantum ESPRESSO code^[31]. We used ultrasoft pseudopotentials^[32] for all atomic species, with plane-wave and charge-density cutoffs of 30 and 300 Ry, respectively. The Perdew-Burke-Ernzerhof (PBE) exchange-correlation functional^[33] was used. Carbon surface structures were based on fully relaxing all atoms within 32-atom, 4×4 hexagonal supercells of graphene, with an initial in-plane lattice parameter of 2.46 Å. A 12×12 Monkhorst-Pack \mathbf{k} -point mesh was used to sample the Brillouin Zone in the relaxed structures, with an applied Gaussian electronic smearing of 0.007 Ry. For the corrugated samples, rippling was induced by decreasing the in-plane lattice parameter perpendicular to the zigzag direction, convoluting the out-of-plane coordinates with a

sinusoidal variation, and relaxing the resulting structure within the compressed unit cell. To compute the XAS spectra, the unit cells were expanded to 8×8 (for the anion-adsorbed and in-plane strained system) and 4×8 (for the rippled system), with the \mathbf{k} -point meshes scaled accordingly. Anion adsorption binding curves and geometries were obtained by fixing the anion distance above the plane and allowing all other degrees of freedom (including those associated with the carbon surface) to relax. The C-C-X bond angles reported in the text represent averages over all three such bonds for each sample.

To account for the bias in the simulated spectra, we applied the effective screening medium method (ESM)^[19], which permits calculations on a charged working electrode while screening the spurious electrostatic interactions that arise from periodicity in standard plane-wave implementations of DFT. The charge on the working electrode was varied to mimic the application of an external bias across electrodes in the *in situ* experiments. Note that the exact relationship between charge and potential bias is difficult to determine theoretically, particularly in the presence of OH⁻ adsorption^[34]. However, if we neglect the effects of specific adsorption at the EDL, then as a rough approximation, a charge of $\pm 0.01 e/\text{atom}$ corresponds to $\sim \pm 0.6$ V half-cell bias with respect to the PZC in a symmetric two-electrode configuration (see supplementary information for details, including Figure S9). The inclusion of ESM was motivated by its recent use in studying space charge-induced quantum capacitance limitations in graphitic electrodes^[2]. The theoretical XAS spectrum of the bias-enabled system was then calculated using the excited-state core hole approximation and the Shirley interpolation scheme, as described in refs [16]^[18] and further elucidated in the supporting information.

Supporting Information:

Supporting Information is available from the Wiley Online Library or from the author.

Acknowledgments: This work performed under the auspices of the U.S. DoE by Lawrence Livermore National Laboratory (LLNL) under Contract DE-AC52-07NA27344 and funded by the LDRD Program at LLNL under project tracking codes 10-LW-045 and 12-ERD-035. Portions of this research were performed on beamlines 7.0.1.1 and 8.0.1.3 at the Advanced Light Source and the Molecular Foundry, Lawrence Berkeley National Laboratory, which is supported by the Director, Office of Science, Office of Basic Energy Sciences, of the U.S. DoE under Contract DE-AC02-05CH11231. BCW, TO, and MO acknowledge support from the Japan-U.S. Cooperation Project for Research and Standardization of Clean Energy Technologies. TvB acknowledges support from the Office of Basic Energy Sciences, Division of Materials Sciences and Engineering. Additional data are available in the supporting information.

- [1] B. Dyatkin, Y. Gogotsi, Faraday Discussions 2014, Advance Article; I. Heller, J. Kong, K. A. Williams, C. Dekker, S. G. Lemay, Journal of the American Chemical Society 2006, 128, 7353.
- [2] B. C. Wood, T. Ogitsu, M. Otani, J. Biener, Journal of Physical Chemistry C 2014, 118, 4.
- [3] A. S. Arico, P. Bruce, B. Scrosati, J. M. Tarascon, W. Van Schalkwijk, Nature Materials 2005, 4, 366; J. R. Miller, P. Simon, Science 2008, 321, 651; P. Simon, Y. Gogotsi, Nature Materials 2008, 7, 845.
- [4] M. Deschamps, E. Gilbert, P. Azais, E. Raymundo-Pinero, M. R. Ammar, P. Simon, D. Massiot, F. Beguin, Nature Materials 2013, 12, 351.
- [5] J. Chmiola, C. Largeot, P.-L. Taberna, P. Simon, Y. Gogotsi, Angewandte Chemie International Edition 2008, 47, 3392; J. Chmiola, G. Yushin, Y. Gogotsi, C. Portet, P. Simon, P. L. Taberna, Science 2006, 313, 1760.
- [6] M. Inagaki, H. Konno, O. Tanaike, Journal of Power Sources 2010, 195, 7880; L. L. Zhang, R. Zhou, X. S. Zhao, J. Mater. Chem. 2010, 20, 5983; Y. W. Zhu, S. Murali, M. D. Stoller, K. J. Ganesh, W. W. Cai, P. J. Ferreira, A. Pirkle, R. M. Wallace, K. A. Cychosz, M. Thommes, D. Su, E. A. Stach, R. S. Ruoff, Science 2011, 332, 1537.
- [7] P. Simon, Y. Gogotsi, Accounts of Chemical Research 2013, 46, 1094.
- [8] J. Biener, S. Dasgupta, L. Shao, D. Wang, M. A. Worsley, A. Wittstock, J. R. I. Lee, M. M. Biener, C. A. Orme, S. O. Kucheyev, B. C. Wood, T. M. Willey, A. V. Hamza, J. Weissmueller, H. Hahn, T. F. Baumann, Advanced Materials 2012, 24, 5083.
- [9] R. K. Kalluri, M. M. Biener, M. E. Suss, M. D. Merrill, M. Stadermann, J. G. Santiago, T. F. Baumann, J. Biener, A. Striolo, Physical Chemistry Chemical Physics 2013, 15, 2309.
- [10] K. Uchida, S. Okada, K. Shiraishi, A. Oshiyama, Physical Review B 2007, 76; J. Xia, F. Chen, J. Li, N. Tao, Nature Nanotechnology 2009, 4, 505.
- [11] S. Dasgupta, D. Wang, C. Kübel, H. Hahn, T. F. Baumann, J. Biener, Advanced Functional Materials 2014.
- [12] J. Stöhr, *NEXAFS Spectroscopy*, Springer, New York 1992.
- [13] Z. Nagy, Journal of Solid State Electrochemistry 2011, 15, 1679; C. Escudero, M. Salmeron, Surface Science 2013, 607, 2.
- [14] P. E. Batson, Physical Review B 1993, 48, 2608.
- [15] L.-H. Shao, J. Biener, H.-J. Jin, M. M. Biener, T. F. Baumann, J. Weissmueller, Advanced Functional Materials 2012, 22, 3029.
- [16] R. A. Rosenberg, P. J. Love, V. Rehn, Physical Review B 1986, 33, 4034.
- [17] P. Hohenberg, W. Kohn, Physical Review 1964, 136, B864; W. Kohn, L. J. Sham, Physical Review 1965, 1, 1697.
- [18] D. Prendergast, S. G. Louie, Physical Review B 2009, 80, 235126; D. Prendergast, G. Galli, Physical Review Letters 2006, 96, 215502.
- [19] M. Otani, O. Sugino, Physical Review B 2006, 73; M. Otani, I. Hamada, O. Sugino, Y. Morikawa, Y. Okamoto, T. Ikeshoji, Physical Chemistry Chemical Physics 2008, 10, 3609.
- [20] A. H. England, A. M. Duffin, C. P. Schwartz, J. S. Uejio, D. Prendergast, R. J. Saykally, Chemical Physics Letters 2011, 514, 187.
- [21] P. J. Lasky, P. H. Lu, M. X. Yang, R. M. Osgood, B. E. Bent, P. A. Stevens, Surface Science 1995, 336, 140.
- [22] K. Suenaga, E. Sandre, C. Colliex, C. J. Pickard, H. Kataura, S. Iijima, Physical Review B 2001, 63.

- [23] F. Baldessari, J. G. Santiago, *Journal of Colloid and Interface Science* 2009, 331, 549.
- [24] J. M. Black, G. Feng, P. F. Fulvio, P. C. Hillesheim, S. Dai, Y. Gogotsi, P. T. Cummings, S. V. Kalinin, N. Balke, *Advanced Energy Materials* 2014, 4, 1300683.
- [25] M. Eikerling, A. A. Kornyshev, E. Lust, *Journal of the Electrochemical Society* 2005, 152, E24.
- [26] T. M. Arruda, M. Heon, V. Presser, P. C. Hillesheim, S. Dai, Y. Gogotsi, S. V. Kalinin, N. Balke, *Energy & Environmental Science* 2013, 6, 225; J. M. Black, G. Feng, P. F. Fulvio, P. C. Hillesheim, S. Dai, Y. Gogotsi, P. T. Cummings, S. V. Kalinin, N. Balke, *Advanced Energy Materials* 2014, 4; C. Merlet, B. Rotenberg, P. A. Madden, P. L. Taberna, P. Simon, Y. Gogotsi, M. Salanne, *Nature Materials* 2012, 11, 306; L. D. Xing, J. Vatamanu, O. Borodin, D. Bedrov, *Journal of Physical Chemistry Letters* 2013, 4, 132; J. Vatamanu, L. L. Cao, O. Borodin, D. Bedrov, G. D. Smith, *Journal of Physical Chemistry Letters* 2011, 2, 2267; C. Merlet, C. Pean, B. Rotenberg, P. A. Madden, P. Simon, M. Salanne, *Journal of Physical Chemistry Letters* 2013, 4, 264.
- [27] J. H. Guo, Y. Luo, A. Augustsson, J. E. Rubensson, C. Sathe, H. Agren, H. Siegbahn, J. Nordgren, *Physical Review Letters* 2002, 89.
- [28] T. Warwick, P. Heimann, D. Mossessian, W. McKinney, H. Padmore, *Review of Scientific Instruments* 1995, 66, 2037.
- [29] J. J. Jia, T. A. Callcott, J. Yurkas, A. W. Ellis, F. J. Himpsel, M. G. Samant, J. Stohr, D. L. Ederer, J. A. Carlisle, E. A. Hudson, L. J. Terminello, D. K. Shuh, R. C. C. Perera, *Review of Scientific Instruments* 1995, 66, 1394.
- [30] J. R. I. Lee, M. Bagge-Hansen, T. M. Willey, R. W. Meulenberg, M. H. Nielsen, I. C. Tran, T. van Buuren, in *Methods in Enzymology*, Vol. 532 (Ed: J. De Yoreo), Academic Press, 2013, 165.
- [31] G. Paolo, et al., *Journal of Physics: Condensed Matter* 2009, 21, 395502.
- [32] D. Vanderbilt, *Physical Review B* 1990, 41, 7892.
- [33] J. P. Perdew, K. Burke, M. Ernzerhof, *Physical Review Letters* 1996, 77, 3865.
- [34] M. D. Radin, T. Ogitsu, M. Otani, J. Biener, B. C. Wood, arXiv:1410.0767 2014.

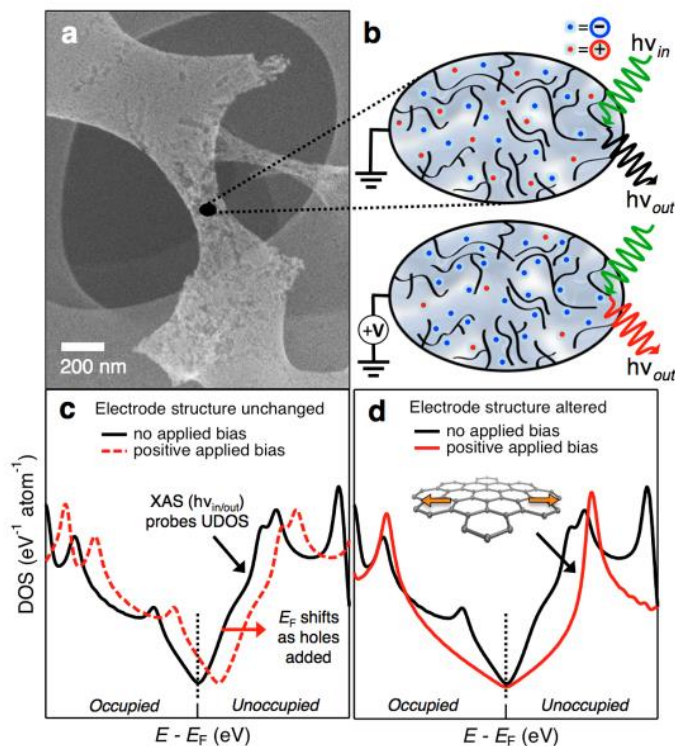


Figure 1. (a) 3D-NG is a model graphitic electrode material comprised of a hierarchical pore structure, as demonstrated by scanning electron microscopy, with (b) ligaments, shown schematically, composed of nanoporous, interconnected, single-layer graphene sheets. Under applied bias, charge is stored in the assembled electric double layer. During charging, bias-induced changes of the electrode's electronic structure (specifically the unoccupied density of states) can be directly interrogated by *in operando* soft x-ray absorption spectroscopy ($h\nu_{in}/h\nu_{out}$). The technique thus provides atomic level insight in the mechanism of bias-induced charge accumulation/depletion by allowing one to differentiate between Fermi level shifts (rigid band approximation, shown in (c) for positive applied bias), and (d) complex changes in electronic structure that mirror altered electrode surface chemistry and morphology.

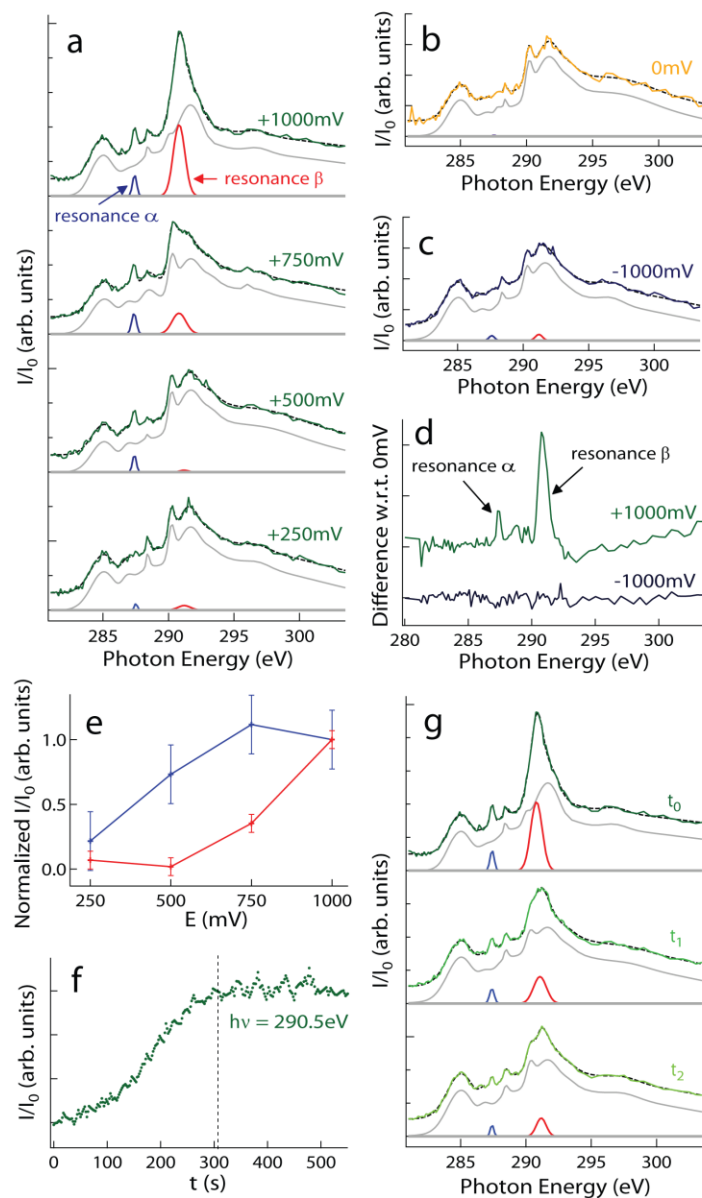


Figure 2. *In operando* carbon K-edge XAS data for a 3D-NG EDLC electrode in 1M NaCl_(aq) under (a) constant DC biases between +250 and +1000 mV (green), (b) zero bias (orange), and (c) -1000 mV (dark blue). Fits to the experimental data in (a) through (c) are obtained via a self-consistent, quasi Monte-Carlo, algorithm (dashed black); two prominent, bias-dependent, subcomponents of the fit are extracted (light blue and red) and displayed with the remainder (gray). (d) Difference spectra of +1000 and -1000 mV with respect to zero bias. (e) Normalized intensity variation of bias-dependent subcomponents of the fit as a function of applied bias. (f) Absorption intensity at $h\nu=290.5$ eV sampled at ~ 1 Hz for 600 s, after bias jump from 0 mV to +1000 mV. (g) Sequentially recorded *in operando* XAS data collected immediately after application of +1000 mV, ($\Delta t_{i,(i+1)} \sim 760$ s for t_0, t_1, t_2). Fits and subcomponents are also displayed (*vide supra*).

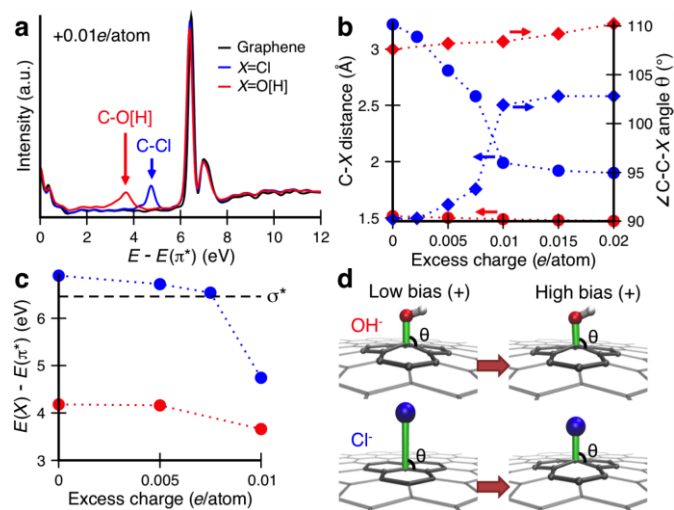


Figure 3. Simulations of specific anion adsorption on a graphene electrode. **(a)** Simulated XAS spectra for pristine graphene (black) and graphene with a Cl⁻ (blue) or OH⁻ (red) adsorbate at an excess system charge of +0.01 e/atom, assuming 10% adsorbate coverage. **(b)** C-X bond length (left axis) and C-C-X bond angle (right axis) for X=[Cl⁻,OH⁻] as a function of excess system charge. **(c)** Predicted energy of the adsorbate-shifted σ^* resonance with respect to the π^* resonance, given as a function of excess system charge. The dashed line indicates the corresponding quantity for pristine graphene. **(d)** Geometric changes in the OH⁻ and Cl⁻ adsorption geometries from low bias (+0.00 e/atom) to high bias (+0.01 e/atom). For Cl⁻, rehybridization is only visible at high positive bias. Excess charge is defined as the total charge on the graphene+X system; within this definition, +0.00 e/atom implies a weak positive charge on graphene due to charge transfer to the X adsorbate that shifts the point of zero charge (PZC).

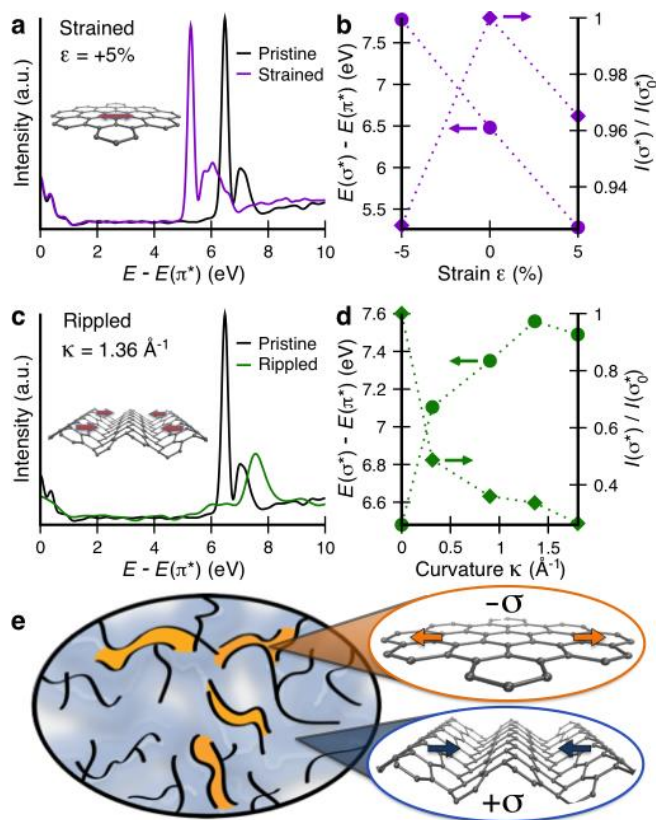


Figure 4. Simulations for graphene with application of compressive or tensile stress. **(a)** Simulated XAS spectra for graphene at equilibrium (black) and under 5% in-plane, uniaxial tensile strain (purple, with geometry shown in inset). **(b)** Predicted energy (left axis, relative to the π^* resonance) and intensity (right axis, relative to the σ^* intensity at zero strain) of the dominant σ^* resonance upon application of in-plane strain, given as a function of applied strain (+/-=tensile/compressive). **(c)** Simulated XAS spectra for flat graphene (black) and corrugated graphene with a maximum curvature of 1.362 \AA^{-1} (green, with geometry shown in inset). **(d)** Predicted energy (left axis, relative to the π^* resonance) and intensity (right axis, relative to the σ^* intensity at zero strain) of the dominant σ^* resonance upon introduction of surface corrugation, given as a function of maximum curvature. **(e)** Schematic of proposed mechanism for planarization of 3D-NG ligaments during charging at positive bias. EDL-induced actuation creates a temporary stress gradient at the boundary between the nanopores (red), where EDL formation is incomplete due to slower diffusion kinetics, and the larger pores (blue), where the equilibrium EDL structure exists. This gradient induces planarization where local tensile stress is experienced. Once charging is complete, the system relaxes so as to neutralize the stress gradient.

Table of Contents Entry: The dynamic physiochemical response of a functioning graphene-based aerogel supercapacitor is monitored *in operando* with soft x-ray spectroscopy and interpreted through *ab initio* atomistic simulations. Unanticipated changes in the electronic structure of the electrode as a function of applied voltage bias indicate structural modifications across multiple length scales via independent pseudocapacitive and electric double layer charge storage channels.

Keywords: *in operando* x-ray spectroscopy, *ab initio* simulation, supercapacitor, carbon aerogel electrode, electronic structure

Michael Bagge-Hansen, Brandon C. Wood, Tadashi Ogitsu, Trevor M. Willey, Ich C. Tran, Arne Wittstock, Monika M. Biener, Matthew D. Merrill, Marcus A. Worsley, Minoru Otani, Cheng-Hao Chuang, David Prendergast, Jinghua Guo, Theodore F. Baumann, Tony van Buuren, Jürgen Biener, Jonathan R. I. Lee*

Potential-induced electronic structure changes in supercapacitor electrodes observed by *in operando* soft x-ray spectroscopy

